Speckle Imaging Characterization of Radial Velocity Exoplanet Systems

Paul A. Dalba[1,12] , Stephen R. Kane[1] , Steve B. Howell[2] , Elliott P. Horch[3] , Zhexing Li[4] , Lea A. Hirsch[5] ,
Jennifer Burt[6] , Timothy D. Brandt[7] , Teo Močnik[8] , Gregory W. Henry[9] , Mark E. Everett[10] , Lee J. Rosenthal[11] , and
Andrew W. Howard[11]

[1] Department of Earth and Planetary Sciences, University of California Riverside, 900 University Avenue, Riverside, CA 92521, USA; pdalba@ucr.edu
[2] NASA Ames Research Center, Moffett Field, CA 94035, USA
[3] Department of Physics, Southern Connecticut State University, New Haven, CT 06515, USA
[4] Department of Earth & Planetary Sciences, University of California Riverside, 900 University Avenue, Riverside, CA 92521, USA
[5] Kavli Institute for Particle Astrophysics and Cosmology, Stanford University, Stanford, CA 94305, USA
[6] Jet Propulsion Laboratory, California Institute of Technology, 4800 Oak Grove Drive, Pasadena, CA 91109, USA
[7] Department of Physics, University of California, Santa Barbara, Santa Barbara, CA 93106, USA
[8] Gemini Observatory/NSF's NOIRLab, 670 N. A'ohoku Place, Hilo, HI 96720, USA
[9] Center of Excellence in Information Systems, Tennessee State University, Nashville, TN 37209, USA
[10] National Optical Astronomy Observatory, Tucson, AZ 85719, USA
[11] Department of Astronomy, California Institute of Technology, Pasadena, CA 91125, USA

Abstract

We conducted speckle imaging observations of 53 stellar systems that were members of long-term radial velocity (RV) monitoring campaigns and exhibited substantial accelerations indicative of planetary or stellar companions in wide orbits. Our observations were made with blue and red filters using the Differential Speckle Survey Instrument at Gemini-South and the NN-Explore Exoplanet Stellar Speckle Imager at the WIYN telescope. The speckle imaging identifies eight luminous companions within $2''$ of the primary stars. In three of these systems—HD 1388, HD 87359, and HD 104304—the properties of the imaged companion are consistent with the RV measurements, suggesting that these companions may be associated with the primary and the cause of the RV variation. For all 53 stellar systems, we derive differential magnitude limits (i.e., contrast curves) from the imaging. We extend this analysis to include upper limits on companion mass in systems without imaging detections. In 25 systems, we rule out companions with masses greater than 0.2 $M_\odot$, suggesting that the observed RV signals are caused by late-M dwarfs or substellar (potentially planetary) objects. On the other hand, the joint RV and imaging analysis almost entirely rules out planetary explanations of the RV signal for HD 19522 and suggests that the companion must have an angular separation below a few tenths of an arcsecond. This work highlights the importance of combined RV and imaging observations for characterizing the outer regions of nearby planetary systems.

1. Introduction

Indirect detection of exoplanets has yielded thousands of new discoveries, thanks largely to the efforts of large-scale surveys that have successfully monitored thousands of stars. In particular, the radial velocity (RV) and transit detection techniques have contributed the bulk of these discoveries via missions such as Kepler (Borucki 2016), the Transiting Exoplanet Survey Satellite (TESS; Ricker et al. 2015), and numerous ground-based surveys (e.g., Christian et al. 2006; Howard et al. 2010; Hojjatpanah et al. 2019). However, the validation of exoplanet candidates can be an expensive endeavor, often requiring follow-up observations with competitive facilities and detailed analyses of ancillary data sets (Santerne et al. 2015; Parviainen et al. 2019; Torres et al. 2017). For RV detections of exoplanet candidates, the use of high-resolution imaging can reveal the presence of stellar companions, thus resolving an inclination ambiguity to the companion mass or the nature of a long-term RV trend (Crepp et al. 2012; Wittrock et al. 2016; Kane et al. 2019b). Such imaging can occasionally reveal the presence of exotic stellar companions, whose low luminosity and RV signature can mimic that of a planet (Crepp et al. 2013; Kane et al. 2019a).

Several RV surveys have now been operating for a few decades, resulting in a sensitivity to long-period companions that are potentially Jupiter and Saturn analogs (Boisse et al. 2012; Rowan et al. 2016; Feng et al. 2019; Wittenmyer et al. 2020). Long-period companions to relatively close stars can translate into large angular separations, enabling the potential for direct detection if the companions are stellar (Cheetham et al. 2018). Even companions in eccentric orbits can be detected since the fraction of the orbit outside of the inner working angle and close to apastron can comprise a substantial fraction of the full orbital period (Kane 2013). Thus, the results of RV surveys for exoplanets published by Butler et al. (2017) present an opportunity to validate numerous exoplanet candidates through a corresponding imaging survey of the host stars. Fortunately, many of these candidates have also been monitored by Rosenthal et al. (2021), providing further constraints on the companion orbits and mass estimates.

Here we present the results of a speckle imaging survey for 53 stars that have proposed substellar companions based on the RV data of Butler et al. (2017) and Rosenthal et al. (2021). Our imaging data are used to constrain the masses of the detected RV companions and search for possible stellar companions. In Section 2 we describe our target sample. In Section 3, we summarize the speckle imaging observations that were conducted

for those stars. Section 4 discusses the utilization of RV orbital solutions in combination with our speckle imaging data. The resulting mass constraints for the detected companions are provided in Section 5. We discuss the implications of our results for current and future exoplanets surveys in Section 6 and provide a summary and concluding remarks in Section 7.

2. Target Sample

Our target list consists of a subset of the systems identified as having planet candidates by Butler et al. (2017) that are also amenable to speckle imaging. We excluded systems that showed significant correlation between the RVs and the stellar activity as determined by the model comparison technique of Butler et al. (2017). Such targets were identified in Table 2 of Butler et al. (2017) as having "activity" as their interpretation. We only chose to observe targets with the interpretation of "candidate," meaning that the planet candidate model was favored over a stellar activity model to 0.1% false-alarm probability.

During the preparation of this paper, many of these systems were further characterized through the California Planet Search (CPS) Legacy Survey, which published decades of RV observations from the High Resolution Echelle Spectrometer (HIRES) at the Keck I telescope (Rosenthal et al. 2021). We have included those results in the following analysis of imaging data.

The stellar properties needed for our analysis included V-band apparent magnitude, distance, and mass (see Table 1). We collected V-band magnitudes for each star from the online Simbad database.[13] The distance to each star was determined using Gaia Data Release 2 (DR2) parallax measurements (Gaia Collaboration et al. 2018) including a prior on distance (Bailer-Jones et al. 2018). We adopted the stellar masses of Rosenthal et al. (2021) for those stars that are members of the CPS Legacy Survey. For the remaining stars, we processed archival HIRES spectra following Fulton et al. (2015) to infer the stellar mass.

3. Speckle Imaging Observations

We summarize the speckle imaging observations in Table 2. Observations were acquired using the Differential Speckle Survey Instrument (DSSI; Horch et al. 2009, 2011) at the Gemini-South Telescope and the NN-Explore Exoplanet Stellar Speckle Imager (NESSI; Scott et al. 2018) at the Wisconsin-Indiana-Yale-NOAO (WIYN) Telescope.

Standard procedure was followed when acquiring speckle imaging observations with either instrument (Horch et al. 2011; Howell et al. 2011). In both cases, the image at the telescope focal plane is collimated and then separated into red and blue components using a dichroic beamsplitter. The light is then collected by two electron-multiplying charge-coupled devices (EMCCDs) using sequences of short (60 ms at Gemini-South, 40 ms at WIYN) exposures. For DSSI, the central wavelength and bandwidth for the blue and red filters are 692 and 40 nm, and 880 and 50 nm, respectively. For NESSI, the central wavelength and bandwidth for the blue and red filters are 562 and 44 nm, and 832 and 40 nm, respectively.

Full descriptions of the reduction and analysis techniques applied to the DSSI and NESSI data are provided by Horch et al. (2011) and Howell et al. (2011), respectively. The reduction

---

[13] http://simbad.u-strasbg.fr/simbad/

Table 1
Summary of the Stellar Properties for the Target Sample

Star	V	d (pc)	$M_\star$ ($M_\odot$)	References
GL 317	11.9	15.197 ± 0.013	0.453 ± 0.009	1
HD 1326	8.1	3.5623 ± 0.0006	0.400 ± 0.008	1
HD 1388	6.51	26.923 ± 0.038	1.027 ± 0.046	1
HD 1461	6.47	23.453 ± 0.031	1.031 ± 0.047	1
HD 3765	7.36	17.926 ± 0.032	0.852 ± 0.033	1
HD 5319	8.05	121.41 ± 0.7	1.53 ± 0.14	2
HD 6558	8.2	81.89 ± 0.42	1.29 ± 0.033	1
HD 6734	6.44	46.73 ± 0.11	0.968 ± 0.091	1
HD 7924	7.17	16.9922 ± 0.0072	0.802 ± 0.033	1
HD 9986	6.77	25.445 ± 0.026	1.032 ± 0.05	1
HD 10436	7.75	13.5098 ± 0.0065	0.632 ± 0.015	1
HD 16160	5.8	7.2339 ± 0.0076	0.752 ± 0.026	1
HD 19522	8.11	102.16 ± 0.81	1.28 ± 0.03	2
HD 24040	7.5	46.62 ± 0.14	1.104 ± 0.053	1
HD 25311	8.28	105.96 ± 0.56	1.4 ± 0.04	2
HD 34445	7.31	46.09 ± 0.1	1.11 ± 0.06	1
HD 42618	6.85	24.336 ± 0.025	0.92 ± 0.046	1
HD 50499	7.21	46.285 ± 0.056	1.253 ± 0.035	1
HD 55696	7.95	77.97 ± 0.18	1.36 ± 0.03	2
HD 68017	6.78	21.573 ± 0.027	0.815 ± 0.014	1
HD 68988	8.2	60.84 ± 0.19	1.172 ± 0.049	1
HD 72490	7.82	126.3 ± 1.1	1.37 ± 0.15	2
HD 75732	5.96	12.586 ± 0.012	0.975 ± 0.045	1
HD 75898	8.03	78.05 ± 0.3	1.29 ± 0.06	2
HD 83443	8.23	40.899 ± 0.063	1.007 ± 0.045	1
HD 87359	7.49	31.268 ± 0.046	0.982 ± 0.05	1
HD 92788	7.31	34.654 ± 0.06	1.076 ± 0.044	1
HD 94834	7.6	98.16 ± 0.64	1.39 ± 0.15	2
HD 95735	7.5	2.5484 ± 0.0059	0.392 ± 0.008	1
HD 99491	6.49	18.199 ± 0.015	1.02 ± 0.044	1
HD 104304	5.54	12.693 ± 0.02	1.026 ± 0.045	1
HD 111031	6.87	31.206 ± 0.051	1.099 ± 0.046	1
HD 114174	6.78	26.355 ± 0.036	0.968 ± 0.044	1
HD 114783	7.56	21.063 ± 0.028	0.867 ± 0.036	1
HD 126614	8.81	73.1 ± 0.25	1.021 ± 0.033	1
HD 129814	7.52	41.95 ± 0.11	0.973 ± 0.043	1
HD 145675	6.61	17.9323 ± 0.0073	0.969 ± 0.042	1
HD 146233	5.49	14.125 ± 0.023	0.995 ± 0.044	1
HD 156668	8.42	24.332 ± 0.017	0.785 ± 0.024	1
HD 180053	7.93	137.04 ± 0.61	2.02 ± 0.05	2
HD 188015	8.24	50.67 ± 0.11	1.043 ± 0.048	1
HD 190406	5.8	17.713 ± 0.022	1.07 ± 0.044	1
HD 195564	5.8	24.746 ± 0.057	1.121 ± 0.034	1
HD 197076	6.43	20.886 ± 0.016	0.979 ± 0.05	1
HD 197162	8.01	141.21 ± 0.68	1.2 ± 0.17	2
HD 202696	8.23	188.5 ± 1.6	1.86 ± 0.24	2
HD 207077	8.24	155.5 ± 1.6	1.35 ± 0.14	2
HD 216520	7.53	19.552 ± 0.011	0.791 ± 0.03	1
HD 217850	8.52	65.8 ± 0.87	1.09 ± 0.05	2
HD 221354	6.76	16.8686 ± 0.0089	0.864 ± 0.027	1
HD 265866	10.1	5.5806 ± 0.002	0.373 ± 0.009	1
HIP 52942 A	9.29	164.1 ± 1.3	1.223 ± 0.072	1
HIP 57050	12.0	11.0143 ± 0.0064	0.374 ± 0.009	1

Note. All distances were adopted from Bailer-Jones et al. (2018). In the references column, 1 refers to masses adopted from Rosenthal et al. (2021), and 2 refers to masses inferred by modeling archival HIRES spectra following Fulton et al. (2015).

---

pipeline for NESSI is based on the one developed for DSSI when it began to be used for exoplanet follow-up observations at WIYN and Gemini observatories. In both cases, reconstructed images with angular resolution near the diffraction limit are created to enable the identification of stellar companions at or beyond $\sim0\rlap{.}''1$

Table 2
Summary of the Imaging Observations

Star	Tel./Inst.	Date (UT)
GL 317	Gemini-S/DSSI	2018 Mar 31
GL 1326	Gemini-S/DSSI	2018 Feb 01
HD 1388	WIYN/NESSI	2017 Sep 03
HD 1461	WIYN/NESSI	2017 Sep 03
HD 3765	WIYN/NESSI	2017 Sep 03
HD 5319	WIYN/NESSI	2017 Sep 03
HD 6558	WIYN/NESSI	2017 Sep 04
HD 6734	WIYN/NESSI	2017 Sep 04
HD 7924	WIYN/NESSI	2017 Sep 04
HD 9986	WIYN/NESSI	2017 Sep 04
HD 10436	WIYN/NESSI	2017 Sep 03
HD 16160	WIYN/NESSI	2018 Feb 02
HD 19522	WIYN/NESSI	2018 Feb 02
HD 24040	WIYN/NESSI	2017 Sep 03
HD 25311	WIYN/NESSI	2018 Feb 06
HD 34445	WIYN/NESSI	2017 Apr 05
HD 42618	WIYN/NESSI	2017 Apr 05
HD 50499	Gemini-S/DSSI	2018 Mar 30
HD 55696	Gemini-S/DSSI	2018 Mar 30
HD 68017	WIYN/NESSI	2017 Mar 13
HD 68988	WIYN/NESSI	2017 Mar 13
HD 72490	WIYN/NESSI	2017 Mar 13
HD 75732	WIYN/NESSI	2018 Feb 03
HD 75898	WIYN/NESSI	2017 Mar 13
HD 83443	Gemini-S/DSSI	2018 Mar 31
HD 87359	WIYN/NESSI	2017 Apr 09
HD 92788	WIYN/NESSI	2017 Apr 09
HD 94834	WIYN/NESSI	2017 Apr 05
HD 95735	WIYN/NESSI	2018 Feb 02
HD 99491	WIYN/NESSI	2017 Apr 05
HD 104304	WIYN/NESSI	2018 Feb 02
HD 111031	WIYN/NESSI	2018 Feb 01
HD 114174	WIYN/NESSI	2017 May 22
HD 114783	WIYN/NESSI	2017 May 22
HD 126614	WIYN/NESSI	2018 Jun 19
	Gemini-S/DSSI	2018 Mar 31
HD 129814	WIYN/NESSI	2017 Mar 13
HD 145675	WIYN/NESSI	2017 Aug 09
HD 146233	WIYN/NESSI	2017 Aug 14
HD 156668	WIYN/NESSI	2017 Aug 12
HD 180053	WIYN/NESSI	2017 Sep 05
HD 188015	WIYN/NESSI	2017 Aug 09
HD 190406	WIYN/NESSI	2017 Aug 12
HD 195564	WIYN/NESSI	2017 Sep 04
HD 197076	WIYN/NESSI	2017 Aug 12
HD 197162	WIYN/NESSI	2017 Sep 02
HD 202696	WIYN/NESSI	2017 Aug 12
HD 207077	WIYN/NESSI	2017 Aug 12
HD 216520	WIYN/NESSI	2017 Sep 03
HD 217850	WIYN/NESSI	2017 Aug 12
HD 221354	WIYN/NESSI	2017 Aug 12
HD 265866	WIYN/NESSI	2017 Apr 05
HIP 52942 A	WIYN/NESSI	2017 Apr 05
HIP 57050	WIYN/NESSI	2017 Apr 09

from the primary star. These companions are found by examining the statistics of local maxima and minima in the image as a function of angular separation from the primary (Horch et al. 2011). In concentric annuli 0″.1 in radius surrounding the primary, we estimate the 5σ detection limit in terms of instrumental magnitude difference (Δm_i) between the primary and a possible

companion, where i is the filter. We assume that Δm_i approaches zero at the diffraction limit. Since we are attempting to discover new companion stars (as opposed to detecting those already known to exist; Horch et al. 2019), this assumption ensures that any companions will produce their own peaks in the image. Any peak that exceeds the 5σ value of Δm_i at a specific angular distance is examined as a possible stellar companion. We consider peaks at similar angular separations in both filters as strong evidence for a stellar companion. However, M-dwarf companions are occasionally only detected in the red filter. In Table 5, we list the 5σ detection limit for each of our target stars at 0″.1 and 1″.0.

We identified luminous companions in the speckle imaging observations of eight stars in the sample. The processed speckle images for these eight systems are shown in Figure 1. The companions are readily detectable by eye for each system. Various observed properties of the companions including the position angle (PA), angular separation (α), and the product of seeing and separation (q'; Horch et al. 2004, 2011) are listed in Table 3. For PA and α, we adopt representative uncertainties from Horch et al. (2019). In Table 3, we also list the proper motion of the primary star in R.A. and decl. (μ_α and μ_δ, respectively) as measured by Gaia (Gaia Collaboration et al. 2018). We recover two known binary systems: HD 126614 (Howard et al. 2010) and HD 195564, which is a member of the Washington Double Star Catalog with observations dating back to 1878 (e.g., Burnham 1879; Lloyd 2002; Tokovinin & Horch 2016). We also note that the speckle imaging was not sensitive enough to detect the known white dwarf companion in the HD 114174 system (Crepp et al. 2013). Lastly, one star in our sample, HIP 52942 A, is a known wide binary star, with a common proper-motion companion almost due west at a separation of 17″.6 (Gaia Collaboration et al. 2018). This companion is well beyond the field of view of our speckle imaging. Instead, our data searched for a tertiary star orbiting the A component of the binary.

We also derive several properties of the imaged companions (Table 4). Once again employing a spectral library (Pickles 1998), the NESSI bandpasses, and the known V-band magnitudes of the primaries, we estimate the spectral types of the companions based on their red and blue NESSI magnitudes. We also estimate the V-band magnitude differences (Δm_V) of the companions.

The magnitude and spectral type estimates in Tables 3 and 4 depend on the photometric accuracy of the speckle imaging, which is known to degrade as a function of angular separation from the primary star (Horch et al. 2011). We quantify this with the q' parameter, which is the product of the seeing and the angular separation (Horch et al. 2004). For systems with $q' \gtrsim 0.6$, Horch et al. (2004) and Horch et al. (2011) have shown that the derived magnitude difference is anomalously large (i.e., the companion is measured to be fainter than it actually is). In these cases, the derived Δm_i values represent upper limits rather than precise values. Even if the magnitude of a companion is relatively uncertain, its existence and angular separation from the primary star are still valuable pieces of information when combined with the RV observations.

The imaged companions in two of the eight systems are detected in both blue and red filters. This color information can be used to check for differences in the modeled and observed properties of the companion via isochrone analysis (Hirsch et al. 2017). Briefly, we use the stellar properties of the primary star (Table 1) to determine its position on isochrones from the Dartmouth Stellar Evolution Database (Dotter et al. 2008). We
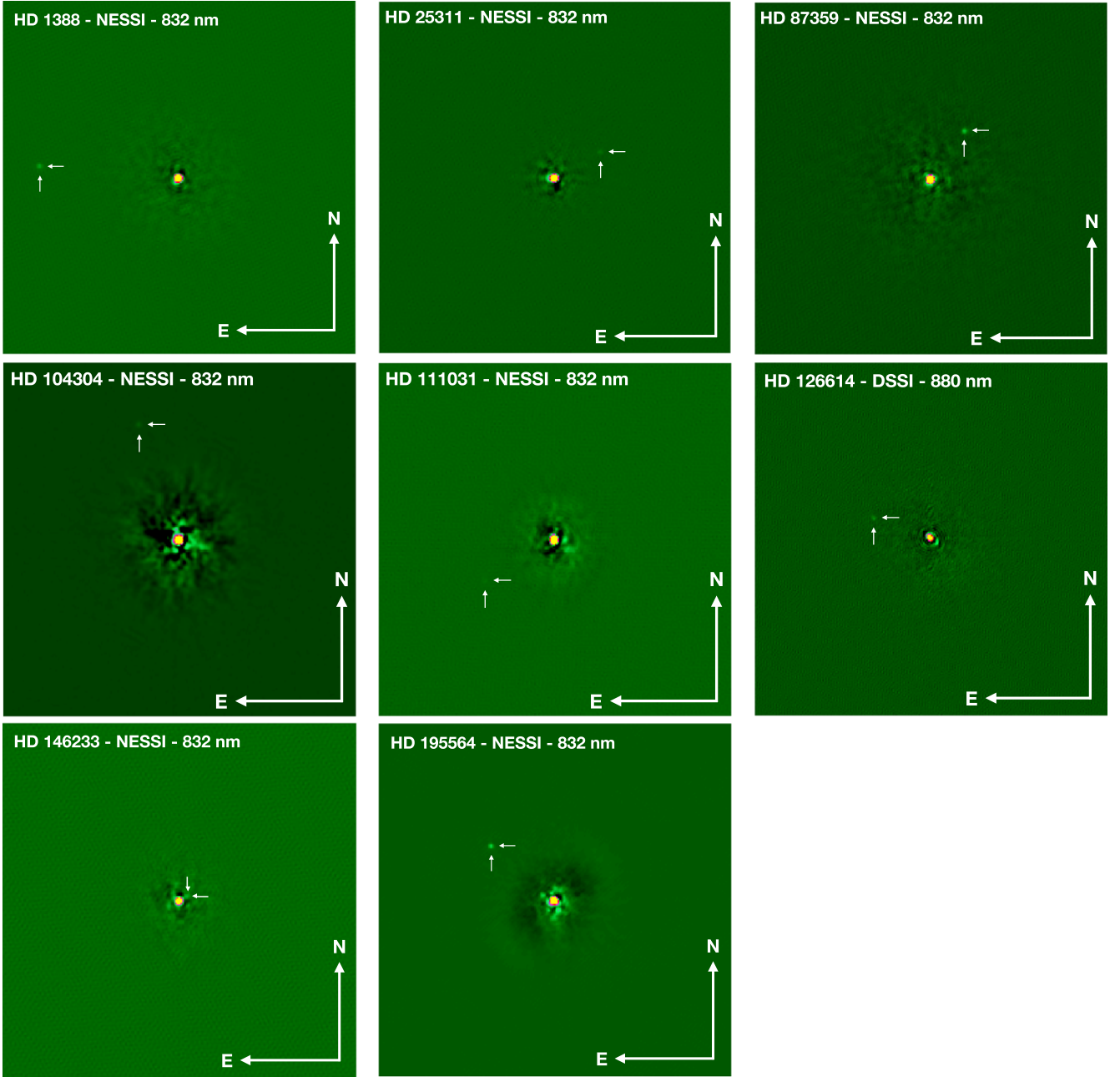
Figure 1. Speckle images for systems with detected companions (indicated by the small arrows). The field of view for each image is $4\rlap{.}''6$ on each side.

then use the observed Δm_i of the neighbor (Table 3) to interpolate down the isochrone to the contrast of a hypothetical bound companion. Each filter provides its own model companion color, which we combine through a weighted average. Finally, comparing the averaged model color to the measured color, we conclude that any offset $\leqslant 3\sigma$ suggests that the off-axis source is likely associated with the primary star.

The results of this isochrone analysis for HD 146233 and HD 195564 are shown in Figure 2. The color offset for the imaged companion of HD 195564 is small and suggests that the companion is likely bound. On the other hand, the imaged companion of HD 146233 is likely not gravitationally bound.

A detection of a companion in HD 146233 was made in each filter. However, there is doubt in the hypothesis that the detection in HD 146233 is a background star. HD 146233 has high proper motion (232 mas yr^1 in R.A., -495 mas yr^{-1} in

decl.; Gaia Collaboration et al. 2018) such that stellar catalogs should have detected a background star with a V-band magnitude of $\sim$9. However, at the location of HD 146233 at the epoch of imaging, the HST Guide Star Catalog (Lasker et al. 1990; Morrison et al. 2001) and the USNO-B1.0 Catalog (Monet et al. 2003) both yield nondetections within $10''$.

It is important to emphasize that it remains possible that our tentative detection for HD 146233 could be spurious. In that case, a possible explanation for our detection is that the limited sample statistics at small angular separations made it difficult to estimate the variance of the residuals and biased that variance estimate low (e.g., Mawet et al. 2014). A noise feature could then have been mistaken as a neighboring star. Further observations of HD 146233 are needed to confirm this result.

In addition to identifying companions, we use the 5σ magnitude limit curves to place upper limits on the mass of
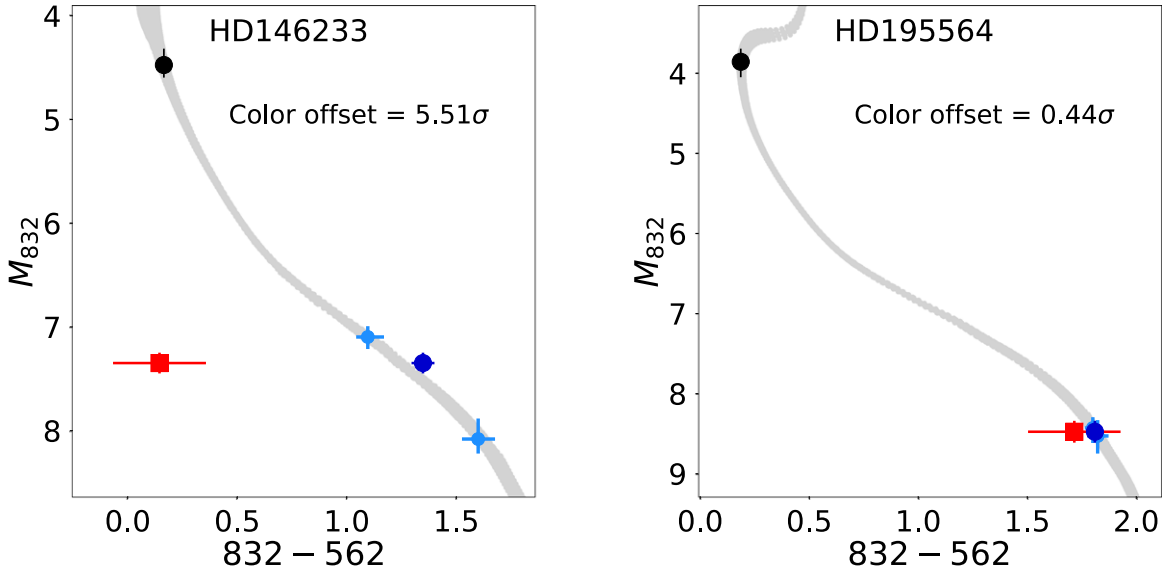
Figure 2. Results of the isochrone analysis (Hirsch et al. 2017) for the imaged companions of HD 146233 (left) and HD 195564 (right). The x-axis is the magnitude difference. The light blue points are the color predictions of the secondary based on the individual measurements of Δm with the primary. The dark blue point is the weighted mean of the light blue points. The substantial offset between the measured (red) and modeled (dark blue) colors of the companion in the HD 146233 system suggests that it is not bound, while the opposite is true for HD 195564, although see the text for a possible caveat for the HD 146233 system.

Table 3
Observed Properties of the Imaged Companions

Star	μ_α (mas yr^{-1})	μ_δ (mas yr^{-1})	Instrument	Filter (nm)	Seeing ($''$)	PA ($°$)	α ($''$)	Δm_i	q' (arcsec^2)
HD 1388	401.216	−0.129	NESSI	832	1.19	85.8 ± 0.6	1.8459 ± 0.0013	4.98	2.197
HD 25311	−4.709	−90.048	NESSI	832	0.36	300.9 ± 0.6	0.6954 ± 0.0013	6.16	0.250
HD 87359	132.648	−207.134	NESSI	832	1.18	324.9 ± 0.6	0.7818 ± 0.0013	4.48	0.923
HD 104304	82.841	−482.807	NESSI	832	0.59	18.9 ± 0.6	1.6238 ± 0.0013	6.65	0.958
HD 111031	−279.792	46.712	NESSI	832	0.45	121.3 ± 0.6	1.0558 ± 0.0013	6.91	0.475
HD 126614	−149.881	−145.915	DSSI	880	0.58	75.7 ± 0.6	0.4830 ± 0.0013	4.82	0.281
			NESSI	832	0.65	76.7 ± 0.6	0.4920 ± 0.0013	4.93	0.318
HD 146233	−11.305	−9.062	NESSI	562	0.72	293.9 ± 0.6	0.1336 ± 0.0013	3.57	0.096
			NESSI	832	0.58	296.1 ± 0.6	0.1334 ± 0.0013	3.59	0.077
HD 195564	309.542	110.075	NESSI	562	0.64	49.4 ± 0.6	1.1130 ± 0.0013	6.20	0.712
			NESSI	832	0.47	49.8 ± 0.6	1.1049 ± 0.0013	4.67	0.519

Note. Proper motions refer to the primary stars. Errors on PA and α are representative based on Horch et al. (2019). For systems with $q' \gtrsim 0.6$ arcsec^2, Δm_i represents an upper limit rather than a precise value. See the text for an explanation.

Table 4
Derived Properties of the Imaged Companions

Star	Spectral Type	Δm_V	Color Offset (σ)
HD 1388	M5	7.8	⋯
HD 25311	M6+	9.0+	⋯
HD 87359	M5	7.1	⋯
HD 104304	M6+	7.5+	⋯
HD 111031	M6+	7.9+	⋯
HD 126614	M6+	7.5+	⋯
HD 146233	K7–M3	3.5–5.7	5.51
HD 195564	M4–M5	6.5–7.5	0.44

Note. A spectral type with a plus sign represents a lower (early-type) limit rather than a single spectral type (i.e., the companion could be a later-type star than listed here). Similarly, ranges in spectral types and Δm_V values are provided when the data from the blue and red filters produce inconsistent results.

possible companions following Kane et al. (2014, 2019b). First, the mass–luminosity relations (Henry & McCarthy 1993) are combined with the known distance to each system to estimate the apparent *V*-band magnitude of a possible stellar companion as a function of mass. The apparent *V*-band magnitude of the primary is known (Table 1), so we calculate the magnitude difference limits (Δm_V) of a possible companion, also as a function of its mass. We then transform Δm_V into magnitude difference limits for blue (Δm_{692} for DSSI and Δm_{562} for NESSI) and red (Δm_{880} for DSSI and Δm_{832} for NESSI) filters using the Pickles spectral library (Pickles 1998) and the transmission curves of each filter. Lastly, the modeled magnitude difference limits are compared to those observed to yield upper mass limits on a companion as a function of angular separation. In Table 5, we list the companion mass limits that correspond to the 5σ instrumental magnitude limit in the blue and red filters. In Figures 3–5, we plot these limits in both filters for a subset of our targets.

4. Literature Radial Velocity Solutions

All of the stars in the sample have received some amount of RV characterization beginning with the analyses published by

Table 5
Summary of 5σ Detection Limits in Magnitude from Speckle Imaging

	Blue Filter (562 nm or 692 nm)				Red Filter (832 nm or 880 nm)			
	Δm		Mass (M_J)		Δm		Mass (M_J)	
Star	0″1	1″0	0″1	1″0	0″1	1″0	0″1	1″0
GL 317	4.66	6.93	159	159	4.45	5.96	159	159
HD 1326	2.59	6.56	202	167	3.56	8.07	167	167
HD 1388	3.02	5.56	721	546	3.96	6.74	557	184
HD 1461	2.12	5.39	808	517	3.77	6.99	472	186
HD 3765	4.41	7.14	420	203	3.58	6.10	203	203
HD 5319	3.37	6.02	872	612	3.26	7.03	669	554
HD 6558	2.82	5.00	864	616	3.50	8.31	633	270
HD 6734	2.79	6.05	937	553	3.79	7.89	593	456
HD 7924	2.56	4.46	644	481	3.36	6.20	311	178
HD 9986	3.51	6.62	653	353	3.27	7.54	574	181
HD 10436	2.67	4.91	554	279	3.31	6.14	201	201
HD 16160	3.11	6.63	555	192	3.90	6.63	192	192
HD 19522	3.18	4.98	847	662	3.90	6.70	604	336
HD 24040	4.06	5.52	633	558	3.98	5.83	531	196
HD 25311	4.28	6.50	723	569	3.93	7.15	659	248
HD 34445	2.53	4.15	819	647	4.18	6.06	504	209
HD 42618	2.72	4.50	735	555	3.64	6.50	482	192
HD 50499	4.95	8.66	548	218	4.61	8.22	302	218
HD 55696	5.02	8.66	573	253	4.44	8.67	509	253
HD 68017	3.62	6.57	620	306	3.00	7.40	580	167
HD 68988	3.60	5.51	683	550	3.79	6.84	578	188
HD 72490	3.57	5.32	887	728	3.54	6.02	775	525
HD 75732	3.21	6.58	613	212	5.19	7.15	212	212
HD 75898	3.62	6.11	753	568	3.52	6.84	669	246
HD 83443	5.51	8.60	237	237	4.97	7.08	237	237
HD 87359	2.52	5.26	719	519	4.54	6.57	228	186
HD 92788	2.55	5.69	776	434	3.93	6.62	421	216
HD 94834	5.52	7.96	658	553	3.56	7.43	641	553
HD 95735	3.83	6.91	162	162	2.75	6.24	162	162
HD 99491	3.40	5.78	640	406	4.01	6.50	281	202
HD 104304	5.43	7.89	434	216	3.65	8.07	390	216
HD 111031	1.24	5.86	942	471	3.27	7.32	615	234
HD 114174	3.14	4.99	675	545	4.00	5.58	492	184
HD 114783	2.55	4.18	650	495	3.99	6.09	181	181
HD 126614	2.28	5.31	774	527	1.93	6.25	774	265
HD 129814	3.57	5.58	672	469	3.45	6.16	531	234
HD 145675	2.92	5.11	659	447	3.53	7.43	398	222
HD 146233	2.88	4.31	716	578	2.92	6.04	609	181
HD 156668	3.33	6.84	556	193	2.79	6.14	372	193
HD 180053	3.81	5.98	882	642	4.30	6.49	579	579
HD 188015	4.14	7.73	593	207	3.36	6.76	531	207
HD 190406	3.24	5.43	702	534	3.47	6.63	590	176
HD 195564	2.51	5.99	874	520	3.33	7.68	656	250
HD 197076	2.88	5.39	698	533	3.45	6.74	499	198
HD 197162	3.28	6.49	963	578	3.18	6.96	728	578
HD 202696	3.14	5.39	1036	770	3.60	6.04	712	607
HD 207077	2.22	4.13	1181	826	2.68	5.07	869	551
HD 216520	1.83	3.48	704	570	3.54	5.58	283	176
HD 217850	3.22	5.03	691	585	3.19	5.67	615	271
HD 221354	3.30	5.34	601	400	3.56	6.71	322	199
HD 265866	2.62	4.79	147	147	3.75	6.05	147	147
HIP 52942 A	2.78	5.84	884	596	3.56	7.23	725	242
HIP 57050	2.84	3.73	162	162	3.00	5.99	162	162

Note. Magnitude limits are given in blue and red instrumental magnitudes. Reference Table 2 for the instrument used to observe each star.

Butler et al. (2017). Many of these stars have since been followed up through more detailed studies of the RV signals (e.g., Vogt et al. 2017; Ment et al. 2018; Luhn et al. 2019;

Trifonov et al. 2019; Burt et al. 2021; Rosenthal et al. 2021). Here, we focus on two categories of RV signals that are complemented by our speckle imaging data: unresolved, long-term RV trends and confirmed Keplerian signals from companions with minimum masses greater than 80 M_J, roughly corresponding to the hydrogen burning limit.

Of the 53 stars in our imaging sample, 4 have known companions with minimum mass greater than 80 M_J and 8 show unresolved trends in their RV time series that are not designated as stellar activity.[14] These trends are quantified as a minimum RV semi-amplitude, which we list in Table 6. The RV trends for seven of these eight stars were identified by the CPS Legacy Survey (Rosenthal et al. 2021). The eighth star with a trend, HD 19522, was not a member of the CPS Legacy Survey, so we measured the trend in the RV time series of HD 19522 as published by Butler et al. (2017).

To constrain the objects causing the RV trends, we estimate the minimum RV semi-amplitude (ΔRV/2) following Kane et al. (2014, 2019b). ΔRV/2 is simply half of the full range of RV observations. For HD 19522, we calculate this value directly. For the remaining nine stars, we use the published acceleration terms from Rosenthal et al. (2021) to reconstruct the RV trend before calculating ΔRV/2. Table 6 lists ΔRV/2 for each of the eight systems considered here.

From this lower limit on RV semi-amplitude, we calculate lower limits on companion mass (M_c) as a function of orbital semimajor axis (a) following

$$\frac{\Delta \mathrm{RV}}{2} \leqslant \sqrt{\frac{G}{a(1 - e^2)}} \frac{M_c \sin i}{\sqrt{M_\star + M_c}}, \tag{1}$$

where $M_\star$ is the mass of the primary star and G is the gravitational constant. In solving Equation (1), eccentricity is drawn from a Beta distribution with shape parameters $s_\alpha = 0.867$ and $s_\beta = 3.03$. This Beta distribution is motivated by empirical trends in the eccentricities of RV exoplanets (Kipping 2013) and is nearly indistinguishable from other empirically motivated distributions (e.g., truncated Rayleigh; Xie et al. 2016). The value of orbital inclination we use in solving Equation (1) is drawn from a distribution uniform in $\cos i$. We take 5000 draws from these distributions, solving Equation (1) each time, to produce distributions of M_c as a function of a. The black lines in Figures 3 and 4 are the median values of these distributions, while the gray shaded regions illustrate the 16th and 84th percentiles. Since ΔRV is a minimum semi-amplitude, the resulting M_c values are minimum masses—but they are not $M \sin i$ values. The uncertainty in the M_c values (i.e., the gray shaded regions) incorporate the unknown inclination and eccentricity of the companion's orbit.

5. Results: Combining Imaging and RV Analyses

The speckle imaging observations (Section 3) and the RV observations (Section 4) place upper and lower limits, respectively, on companion masses. Combining the two can potentially rule out substantial regions of parameter space in the mass–semimajor-axis plane that the companion could occupy. Montet et al. (2014) applied a rigorous likelihood

---

[14] Rosenthal et al. (2021) published linear trends for HD 34445 and HD 156668, which are members of our target sample. However, these trends are likely due to stellar activity as determined by emission in the Ca II H & K lines measured in the same HIRES spectra as the RVs.
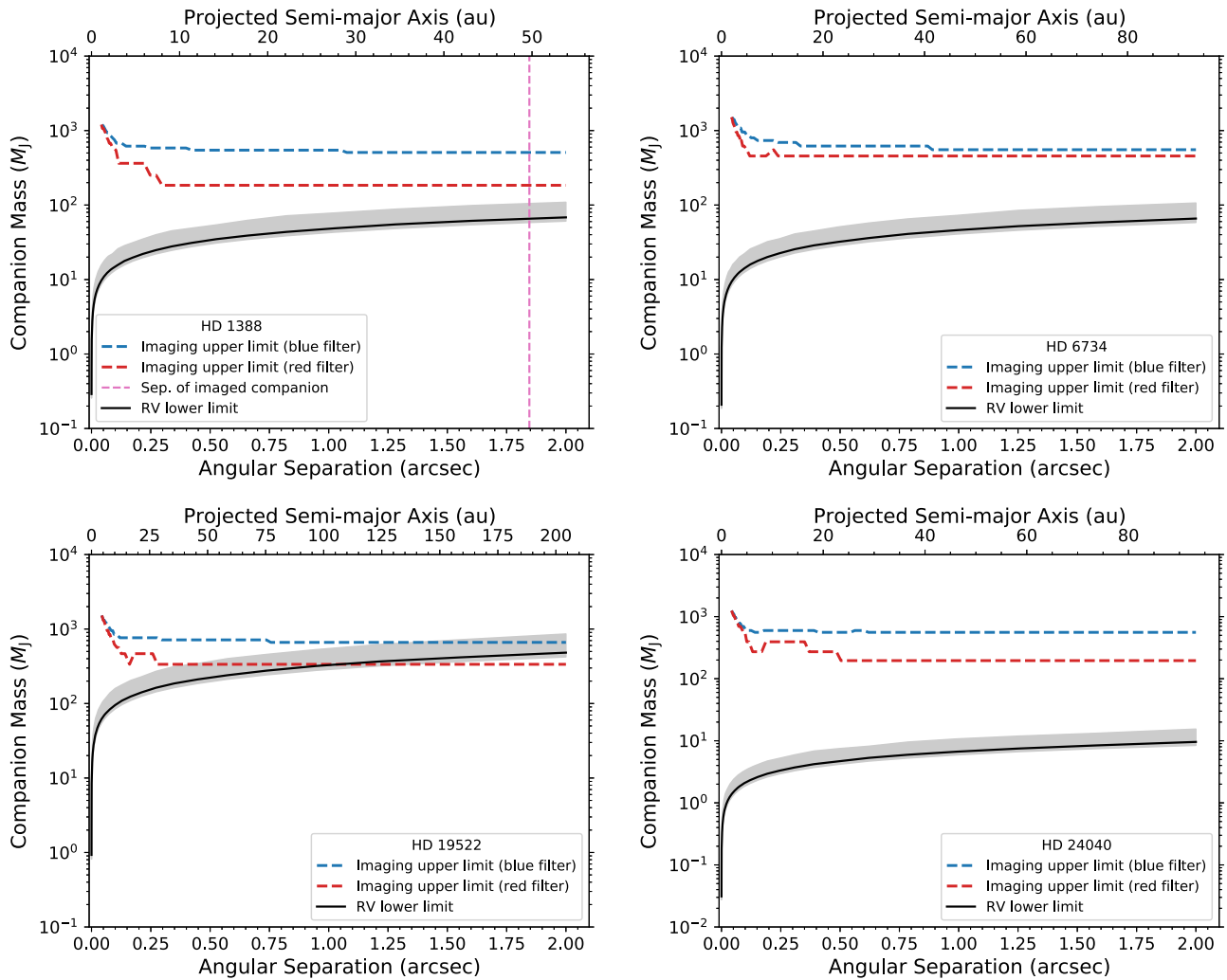
Figure 3. Imaging and RV comparison for four of the eight systems with unresolved RV trends. The blue and red lines correspond to companion upper mass limits (ignoring any detected companion) based on the imaging observations. If a companion was detected, its separation is indicated by the vertical dashed line. The black line and gray shaded region correspond to the lower mass limit distributions (median and 16th–84th percentiles) for the object causing the RV trend. These distributions capture the uncertainty introduced by the unknown inclination and eccentricity of the object's orbit.

analysis that involved marginalizing over eccentricity and inclination to determine the most probable masses and semimajor axes a companion could have, given the data. Kane et al. (2019b) applied a simplified variation on this approach using the measured RV trend to place a limit on RV semi-amplitude. Here, we have followed the latter procedure as described in Section 4.

The lower limits on the companion mass from the RV data are calculated as functions of the semimajor axis (a), while the upper limits on the companion mass from the imaging data are calculated as a function of angular separation (α). By placing both coordinates on the panels in Figures 3–5, we make the assumption that these two coordinates are related by $\alpha = a/d$, where α is expressed in arcseconds, a is expressed in astronomical units, and d is the distance to the host star expressed in parsecs. This assumption neglects the unknown orbital inclination and longitude of periastron of any imaged companion. Therefore, special consideration is required in their interpretation.

The combination of imaging and RV analysis for several systems with RV trends (Figures 3 and 4) places tight constraints on the properties of the companions causing the

trends. Specifically, this applies to HD 19522, HD 114174, and HD 129814. For these systems, there is only a narrow area of mass–separation parameter space in which the companion can exist, and it is unlikely that the companion causing the RV trend is planetary or that it has an orbit with a maximum angular separations beyond $\sim$1″. Similarly, if the imaged companions we detected for HD 1388 and HD 195564 (Figures 3 and 4, vertical dashed lines) are responsible for the RV trends in these systems, then we find that their masses must be at least $\sim$60 M_J and $\sim$90 M_J, respectively. This is consistent with our characterization of the detected companions (Table 4).

For HD 6734, HD 24040, and HIP 57050, the combined imaging and RV constraints still leave a wide area of parameter space available for the properties of the companion. Improved characterization for this system and the others listed above through continued RV observations (i.e., until quadrature is observed) or deeper imaging observations would be useful.

In the cases of the four systems with known RV companions of minimum mass 80 M_J (Figure 5), we can make additional inferences about the companion properties. Since the orbital semimajor axes and eccentricities are known precisely, we can
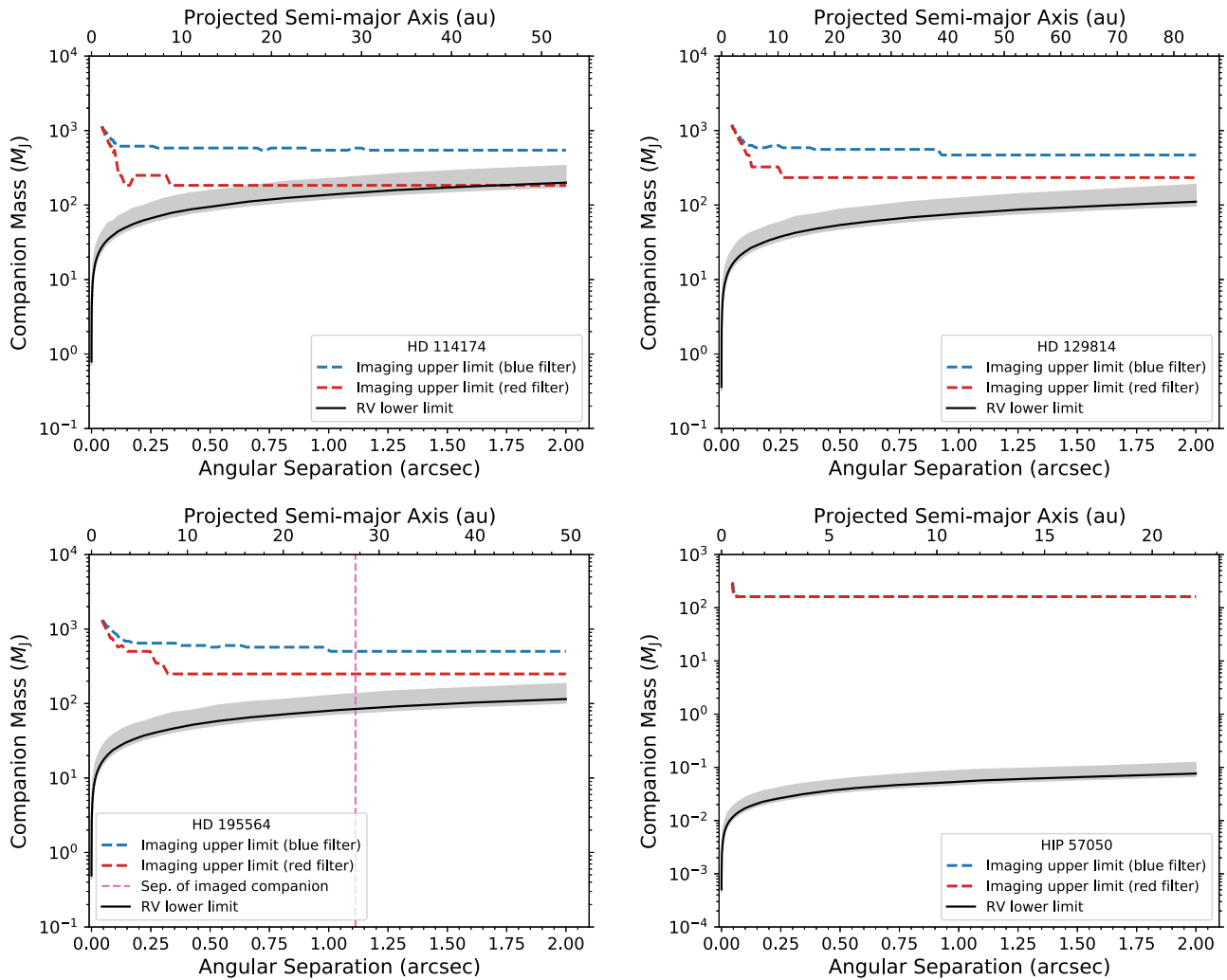
Figure 4. Imaging and RV comparison for the remaining four systems with unresolved RV trends. The description is otherwise identical to Figure 3.

determine the maximum possible angular separations that the companions could have. In Figure 5, this is shown as an orange data point with an arrow pointing toward smaller separations. The error bars in the vertical axis are representative of the measured uncertainty in minimum companion mass. For HD 6558, the upper limits from the speckle imaging suggest that the 68% confidence interval in minimum companion mass is representative of the likely companion's true mass (i.e., not just a lower limit). Therefore, the companion's orbit is more likely to be more edge-on ($\sin i \approx 1$) than face-on ($\sin i \approx 0$).

For HD 87359 and HD 104304, the RV companion minimum mass is known, and we detected a luminous companion (Figure 5, vertical dashed line). In both cases, the angular separation of the imaged companion is smaller than the maximum possible separation of the RV companion, suggesting that these two signals may indeed be caused by the same object. For both systems for which this is true, the companions have stellar masses.

6. Discussion

The transit method, while a successful avenue of planet discovery (e.g., Thompson et al. 2018), is severely limited by observational biases (e.g., Beatty & Gaudi 2008) such that only a few transiting planets on astronomical unit-scale orbits are known (e.g., Wang et al. 2015; Kawahara & Masuda 2019; Dalba & Tamburo 2019). RV surveys, on the other hand, maintain sensitivity out to wider orbital separation. Combined with decade-long baselines of stable observations, the longest running RV surveys (e.g., Tinney et al. 2001; Butler et al. 2017; Rosenthal et al. 2021; Wittenmyer et al. 2020) are beginning to achieve sensitivity to signals resembling the giant planets in our solar system. Imaging follow-up to long-term RV surveys, such as we have presented here, plays a crucial role in validating the signals of wide-orbit planetary or stellar companions, especially if full orbits have not been resolved. By discovering previously unknown stellar companions and placing detection limits (Table 5) in systems with substantial RV acceleration, we have provided important information to supplement our understanding of planet occurrence on wide orbits.

Our results are broadly in line with similar efforts to combine imaging and RV data sets for the characterization of exoplanets, (e.g., Kane et al. 2014; Wittrock et al. 2016, 2017; Kane et al. 2019b), brown dwarfs (e.g., Crepp et al. 2016), and white dwarfs (e.g., Crepp et al. 2018; Kane et al. 2019a). In our case, we have identified systems where the suspected planetary signal is fully consistent with a stellar companion (e.g., HD 1388, HD 87359, and HD 104304) or where no companion is detected and the majority of the remaining parameter space for a companion is
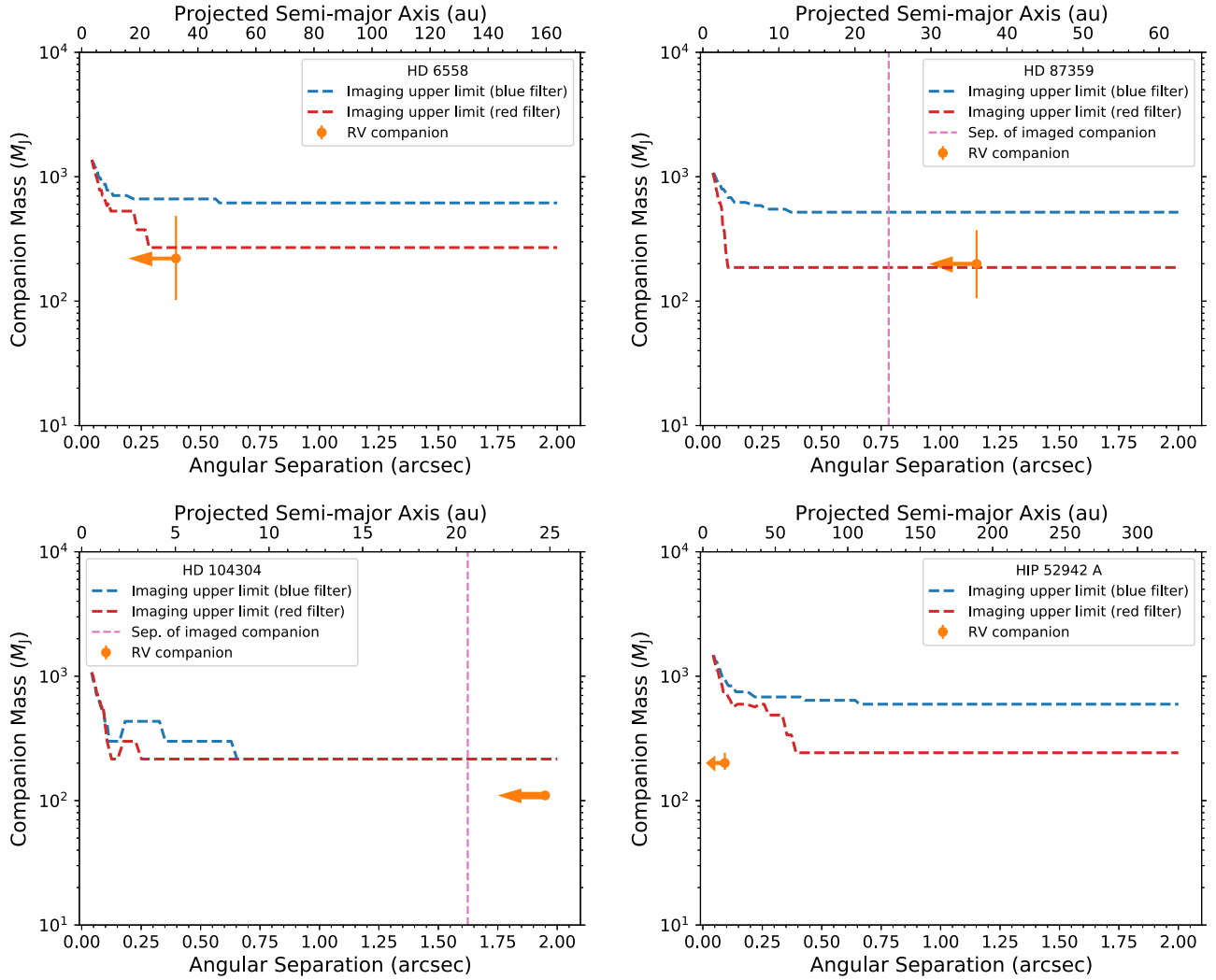
Figure 5. Imaging and RV comparison for systems with RV companions with minimum mass greater than 80 M_J. The blue and red lines correspond to companion upper mass limits (ignoring any detected companion) based on the imaging observations. If a companion was detected, its separation is indicated by the vertical dashed line. The orange data point shows the 68% confidence interval for the mass of the RV companion. It is plotted at the maximum possible angular separation, given the known semimajor axis and orbital eccentricity. If a detected companion is within this separation, then it is consistent with the RV signal.

Table 6
Summary of Systems with Unresolved RV Signals

Star	$\frac{1}{2}\Delta$ RV (m s^{-1})
HD 1388	230
HD 6734	172
HD 19522	657
HD 24040	24
HD 114174	655
HD 129814	297
HD 195564	377
HIP 57050	1

Note. ΔRV/2 is equal to half the total span of the RVs for a given target, which represents a minimum estimate of the RV semi-amplitude. For all stars except HD 19522, this value was derived from the RV acceleration parameters of Rosenthal et al. (2021). For HD 19522, this value was directly measured from the RVs published by Butler et al. (2017).

substellar and planetary (e.g., HD 24040 and HIP 57050). For stars without detected companions at wide separations, the upper limit provided by the speckle imaging flattens to a single value. We show a histogram of these upper limits in Figure 6. For 25

systems, we rule out companions with masses greater than 0.2 $M_\odot$, leaving only late-M dwarfs or substellar objects to explain the RV signals. In the interest of planet and brown dwarf discovery, these 25 systems, which can be identified in Table 5, should be prioritized for continued RV monitoring.

Stellar binaries are a source of confusion for transit and RV surveys alike. For the former, pixels that subtend many arcseconds (as in the case of TESS) can hide stellar companions leading to the inference of erroneous stellar and planetary properties, including radius and density (e.g., Furlan & Howell 2017, 2020; Ziegler et al. 2020). For the latter, the unknown orbital inclination of objects causing long-term accelerations can allow stellar companions to contaminate exoplanet catalogs if an edge-on geometry is assumed (e.g., Kiefer et al. 2021). Therefore, direct imaging serves as a practical false-positive checking practice as well.

The combination of imaging and RV data is a useful technique for exploring the properties of massive companions in nearby star systems, as demonstrated in this work and by others (e.g., Kane et al. 2019b). Including astrometric observations from missions such as Hipparcos and Gaia (e.g., Brandt et al. 2019) provides even more leverage in the characterization of companions. This includes testing for the unfortunate scenario of a photometric
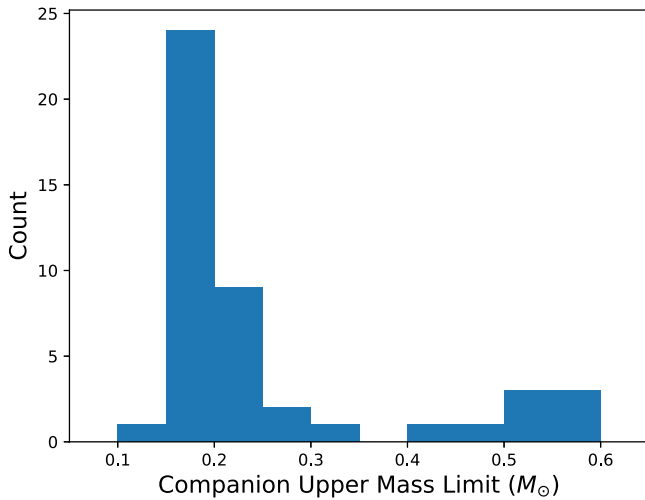
Figure 6. Upper mass limits for secondary stars at wide separations for systems without a detected companion. In 25 systems, we rule out secondaries with masses greater than 0.2 $M_\odot$.

nondetection of an otherwise detectable companion that was near conjunction with the primary at the time of observation. Several of the systems in which we detected a stellar companion do have significant astrometric signals in Hipparcos and Gaia data (Brandt 2018). We leave the joint analysis of the RVs, imaging, and astrometry to a future analysis that will measure precise masses and orbits for these companions.

7. Conclusions

We conducted speckle imaging of 53 stars using instruments at the WIYN and Gemini-South telescopes. The systems had previously been the targets of long-term RV campaigns (Butler et al. 2017; Rosenthal et al. 2021). We focused on systems that exhibited long-term RV trends or companions with measured minimum mass greater than 80 M_J, roughly corresponding to the hydrogen burning limit. However, we also provide companion detection limits in multiple filters for all of our imaging targets (Table 5). Our analysis yielded the following findings.

1. We detected luminous companions in our speckle images of eight systems including HD 1388, HD 25311, HD 87359, HD 104304, HD 111031, HD 126614, HD 146233, and HD 195564. HD 126614 (Howard et al. 2010) and HD 195564 (e.g., Burnham 1879; Lloyd 2002; Tokovinin & Horch 2016) were known binary systems previously.
2. The color information we obtained for HD 146233 and HD 195564 enabled an isochrone analysis suggesting that the imaged companion in HD 195564 (at $\alpha = 1\rlap{.}''1$) is likely gravitationally bound to the primary while the imaged companion in HD 146233 (at $\alpha = 0\rlap{.}''13$) is likely not. Interestingly, neither the HST Guide Star catalog nor the USNO-B catalog detect a background star at the expected brightness or position that could explain the HD 146233 detection. We emphasize that it remains possible that our tentative detection for HD 146233 could be spurious. Further observations are needed to confirm this result.
3. In the cases of HD 1388, HD 87359, and HD 104304, the properties of the imaged companions are consistent with the RV measurements, providing support to the idea that these companions are associated with the primary stars.

4. For HD 6558, our speckle imaging observations provide evidence that the RV companion's orbital inclination is likely to be more edge-on rather than face-on.
5. In several systems with long-term RV trends (HD 19522 and HD 129814), we do not detect luminous companions through our speckle imaging, but the corresponding limits on companion mass rule out planetary scenarios.

Our findings demonstrate the utility of synthesizing imaging and RV data sets for characterizing exoplanetary systems. For stars that are subject to long-term RV monitoring, the presence (or lack thereof) of stellar companions is vital information that is necessary to piece together the formation history of the system. The explanations of the RV trends we provide here are useful for understanding the population of exoplanets at wide orbits as well as making choices about future long-term RV monitoring efforts. Additionally, in all cases, the predictions made by our observations can be tested through additional RV monitoring and deeper imaging campaigns.

During the preparation of this manuscript, Gonzales et al. (2020) identified neighboring stars in the HD 1388 and HD 111031 systems.

ORCID iDs

Paul A. Dalba ⓘ https://orcid.org/0000-0002-4297-5506
Stephen R. Kane ⓘ https://orcid.org/0000-0002-7084-0529
Steve B. Howell ⓘ https://orcid.org/0000-0002-2532-2853
Elliott P. Horch ⓘ https://orcid.org/0000-0003-2159-1463

Zhexing Li ⓘ https://orcid.org/0000-0002-4860-7667
Lea A. Hirsch ⓘ https://orcid.org/0000-0001-8058-7443
Jennifer Burt ⓘ https://orcid.org/0000-0002-0040-6815
Timothy D. Brandt ⓘ https://orcid.org/0000-0003-2630-8073
Teo Močnik ⓘ https://orcid.org/0000-0003-4603-556X
Gregory W. Henry ⓘ https://orcid.org/0000-0003-4155-8513
Mark E. Everett ⓘ https://orcid.org/0000-0002-0885-7215
Lee J. Rosenthal ⓘ https://orcid.org/0000-0001-8391-5182
Andrew W. Howard ⓘ https://orcid.org/0000-0001-8638-0320

References

Bailer-Jones, C. A. L., Rybizki, J., Fouesneau, M., Mantelet, G., & Andrae, R. 2018, AJ, 156, 58
Beatty, T. G., & Gaudi, B. S. 2008, ApJ, 686, 1302
Boisse, I., Pepe, F., Perrier, C., et al. 2012, A&A, 545, A55
Borucki, W. J. 2016, RPPh, 79, 036901
Brandt, T. D. 2018, ApJS, 239, 31
Brandt, T. D., Dupuy, T. J., & Bowler, B. P. 2019, AJ, 158, 140
Burnham, S. W. 1879, MmRAS, 44, 141
Burt, J., Feng, F., Holden, B., et al. 2021, AJ, 161, 10
Butler, R. P., Vogt, S. S., Laughlin, G., et al. 2017, AJ, 153, 208
Cheetham, A., Ségransan, D., Peretti, S., et al. 2018, A&A, 614, A16
Christian, D. J., Pollacco, D. L., Skillen, I., et al. 2006, MNRAS, 372, 1117
Crepp, J. R., Gonzales, E. J., Bechter, E. B., et al. 2016, ApJ, 831, 136
Crepp, J. R., Gonzales, E. J., Bowler, B. P., et al. 2018, ApJ, 864, 42
Crepp, J. R., Johnson, J. A., Howard, A. W., et al. 2012, ApJ, 761, 39
Crepp, J. R., Johnson, J. A., Howard, A. W., et al. 2013, ApJ, 774, 1
Dalba, P. A., & Tamburo, P. 2019, ApJL, 873, L17
Dotter, A., Chaboyer, B., Jevremović, D., et al. 2008, ApJS, 178, 89
Feng, F., Anglada-Escudé, G., Tuomi, M., et al. 2019, MNRAS, 490, 5002
Fulton, B. J., Collins, K. A., Gaudi, B. S., et al. 2015, ApJ, 810, 30
Furlan, E., & Howell, S. B. 2017, AJ, 154, 66
Furlan, E., & Howell, S. B. 2020, ApJ, 898, 47
Gaia Collaboration, Brown, A. G. A., Vallenari, A., et al. 2018, A&A, 616, A1
Gonzales, E. J., Crepp, J. R., Bechter, E. B., et al. 2020, ApJ, 893, 27
Henry, T. J., & McCarthy, Donald W. J. 1993, AJ, 106, 773
Hirsch, L. A., Ciardi, D. R., Howard, A. W., et al. 2017, AJ, 153, 117
Hojjatpanah, S., Figueira, P., Santos, N. C., et al. 2019, A&A, 629, A80
Horch, E. P., Meyer, R. D., & van Altena, W. F. 2004, AJ, 127, 1727
Horch, E. P., Tokovinin, A., Weiss, S. A., et al. 2019, AJ, 157, 56
Horch, E. P., van Altena, W. F., Howell, S. B., Sherry, W. H., & Ciardi, D. R. 2011, AJ, 141, 180
Horch, E. P., Veillette, D. R., Baena Gallé, R., et al. 2009, AJ, 137, 5057
Howard, A. W., Johnson, J. A., Marcy, G. W., et al. 2010, ApJ, 721, 1467
Howell, S. B., Everett, M. E., Sherry, W., Horch, E., & Ciardi, D. R. 2011, AJ, 142, 19
Kane, S. R. 2013, ApJ, 766, 10
Kane, S. R., Dalba, P. A., Horner, J., et al. 2019a, ApJ, 875, 74
Kane, S. R., Dalba, P. A., Li, Z., et al. 2019b, AJ, 157, 252
Kane, S. R., Howell, S. B., Horch, E. P., et al. 2014, ApJ, 785, 93
Kawahara, H., & Masuda, K. 2019, AJ, 157, 218
Kiefer, F., Hébrard, G., Lecavelier, A., et al. 2021, A&A, 645, A7
Kipping, D. M. 2013, MNRAS, 434, L51
Lasker, B. M., Sturch, C. R., McLean, B. J., et al. 1990, AJ, 99, 2019
Lloyd, J. P. 2002, PhD Thesis, Univ. California, Berkeley
Luhn, J. K., Bastien, F. A., Wright, J. T., et al. 2019, AJ, 157, 149
Mawet, D., Milli, J., Wahhaj, Z., et al. 2014, ApJ, 792, 97
Ment, K., Fischer, D. A., Bakos, G., Howard, A. W., & Isaacson, H. 2018, AJ, 156, 213
Monet, D. G., Levine, S. E., Canzian, B., et al. 2003, AJ, 125, 984
Montet, B. T., Crepp, J. R., Johnson, J. A., Howard, A. W., & Marcy, G. W. 2014, ApJ, 781, 28
Morrison, J. E., Röser, S., McLean, B., Bucciarelli, B., & Lasker, B. 2001, AJ, 121, 1752
Parviainen, H., Tingley, B., Deeg, H. J., et al. 2019, A&A, 630, A89
Pickles, A. J. 1998, PASP, 110, 863
Ricker, G. R., Winn, J. N., Vanderspek, R., et al. 2015, JATIS, 1, 014003
Rosenthal, L. J., Fulton, B. J., Hirsch, L. A., et al. 2021, ApJS, in press
Rowan, D., Meschiari, S., Laughlin, G., et al. 2016, ApJ, 817, 104
Santerne, A., Díaz, R. F., Almenara, J. M., et al. 2015, MNRAS, 451, 2337
Scott, N. J., Howell, S. B., Horch, E. P., & Everett, M. E. 2018, PASP, 130, 054502
Thompson, S. E., Coughlin, J. L., Hoffman, K., et al. 2018, ApJS, 235, 38
Tinney, C. G., Butler, R. P., Marcy, G. W., et al. 2001, ApJ, 551, 507
Tokovinin, A., & Horch, E. P. 2016, AJ, 152, 116
Torres, G., Kane, S. R., Rowe, J. F., et al. 2017, AJ, 154, 264
Trifonov, T., Stock, S., Henning, T., et al. 2019, AJ, 157, 93
Vogt, S. S., Butler, R. P., Burt, J., et al. 2017, AJ, 154, 181
Wang, J., Fischer, D. A., Barclay, T., et al. 2015, ApJ, 815, 127
Wittenmyer, R. A., Wang, S., Horner, J., et al. 2020, MNRAS, 492, 377
Wittrock, J. M., Kane, S. R., Horch, E. P., et al. 2016, AJ, 152, 149
Wittrock, J. M., Kane, S. R., Horch, E. P., et al. 2017, AJ, 154, 184
Xie, J.-W., Dong, S., Zhu, Z., et al. 2016, PNAS, 113, 11431
Ziegler, C., Tokovinin, A., Briceño, C., et al. 2020, AJ, 159, 19